



**HAL**  
open science

## Remote sensing and surface observations of the response of the atmospheric boundary layer to a solar eclipse

Fanny Girard-Ardhuin, Bruno Bénéch, Bernard Campistron, Jean Dessens,  
Sandra Jacoby-Koaly

► **To cite this version:**

Fanny Girard-Ardhuin, Bruno Bénéch, Bernard Campistron, Jean Dessens, Sandra Jacoby-Koaly. Remote sensing and surface observations of the response of the atmospheric boundary layer to a solar eclipse. *Boundary-Layer Meteorology*, 2003, 106, pp.93-115. 10.1023/A:1020837400800 . hal-00139081

**HAL Id: hal-00139081**

**<https://hal.science/hal-00139081>**

Submitted on 27 Oct 2021

**HAL** is a multi-disciplinary open access archive for the deposit and dissemination of scientific research documents, whether they are published or not. The documents may come from teaching and research institutions in France or abroad, or from public or private research centers.

L'archive ouverte pluridisciplinaire **HAL**, est destinée au dépôt et à la diffusion de documents scientifiques de niveau recherche, publiés ou non, émanant des établissements d'enseignement et de recherche français ou étrangers, des laboratoires publics ou privés.



Distributed under a Creative Commons Attribution 4.0 International License

# REMOTE SENSING AND SURFACE OBSERVATIONS OF THE RESPONSE OF THE ATMOSPHERIC BOUNDARY LAYER TO A SOLAR ECLIPSE

FANNY GIRARD-ARDHUIN\*, B. BÉNECH, B. CAMPISTRON, J. DESSENS and S. JACOBY-KOALY

*Laboratoire d'Aérodynamique, OMP, UMR UPS/CNRS 5560, 65300 Campistrous, France*

**Abstract.** On 11 August 1999, a near-total solar eclipse (80%) was observed in Campistrous, France. The influence of this particular event on the atmospheric boundary layer was observed with a UHF-RASS radar, a sodar and an instrumented mast. The changes in turbulence intensity, radar reflectivity, and temperature on the radiative budget are described in relation to collocated ground meteorological data. The impact of the eclipse induces a clear response of the atmosphere, with a time lag of 15 to 30 min, perceptible in several mean and turbulent meteorological variables up to the top of the atmospheric boundary layer.

**Keywords:** Atmospheric boundary layer, Remote sensing, Solar eclipse, UHF-RASS radar.

## 1. Introduction

Solar eclipses are unique opportunities for studying atmospheric phenomena due to changes in the incoming solar radiation occurring faster than during a normal diurnal cycle. During a normal day overland, a convective atmospheric boundary layer (ABL) develops reaching a quasi-steady state in the afternoon with a mixed layer from the ground up to the interfacial layer with the free atmosphere, a region of strong thermal inversion. Generally, the ABL afternoon/evening transition is marked before sunset by a development of a surface inversion related to surface cooling. The convective ABL, often called the residual layer after sunset, becomes neutral above that stable layer. After sunrise, the stable layer is destroyed and a new mixing layer develops. These phenomena have been extensively studied experimentally and theoretically in steady state but the evolution during transitions is not so well known. During the eclipse, the two transitions are reproduced with time scales much shorter than those of the normal diurnal cycle.

The most obvious effects of a partial, annular or total solar eclipse are the significant changes of the surface energy balance and its principal components, the net radiation, the sensible heat, the latent heat and the subsurface heat fluxes as observed during the day/night transitions. These effects on the ABL depend on the duration and intensity of the obscuration.

\* E-mail: fanny\_ardhuin@hotmail.com

As discussed below, the most dramatic meteorological impact is the change in temperature, which was observed during different eclipse events. Some weaker dynamical effects have also been reported. The stability of the surface layer is modified and in many cases, the convective ABL can become neutral or stable. This has a strong impact on turbulence in the ABL and, via air refractive index irregularities, is a source of radar echoes. Quasi-stationarity clearly fails when external forcings such as the sensible heat flux at the surface decrease due to the progressive interception of the solar radiation. The convective turbulence declines with the sensible heat flux, upsetting the previous equilibrium, so that the internal dynamics of turbulence should be taken into account to describe the time evolution of the ABL.

Most of the earlier studies investigated the temperature fall. Segal et al. (1996) described the evolution of the shelter air temperature during a solar eclipse on 10 May 1994. The eclipse was observed in the central United States (89% totality) in the morning during ABL growth. They present a typical change of temperature during the eclipse with three stages (stabilization of the temperature, temperature decrease and temperature increase) corresponding to three regimes of stability. This evolution, observed in different places, is compared with numerical model simulations of the spatial and temporal patterns of the temperature drop. During the same event, Eaton et al. (1997) showed the eclipse effects in the ABL over a desert site in New Mexico, U.S.A. (94% totality), using data acquired near the ground and in the surface layer with a frequency-modulated continuous wave (FM-CW) radar. They report that at the eclipse maximum, the sensible heat flux and the radiation flux were affected, the turbulence was reduced and the air refractive index structure constant decreased dramatically.

Changes in the energy and radiation budget during an eclipse were also described by Stewart and Rouse (1974) for the 10 July 1972 eclipse (90% totality) in the early afternoon in the Arctic. During this particular experiment, they reported also a change of wind intensity and direction.

From measurements made with a 10-cm wavelength radar during a partial eclipse in Oklahoma (U.S.A.), Rabin and Doviak (1989) showed that the radar reflectivity variations follow the variations of solar radiation. They reviewed the different mechanisms for the change in reflectivity and established a relation between the radar reflectivity and the surface sensible and latent heat fluxes. However, they attributed most of the radar reflectivity change to the peculiar behaviour of biological targets such as insects, mainly responsible, according to them, to the clear air radar signal.

Nieuwstadt and Brost (1986) analyzed the decay of convective turbulence in the ABL using a large-eddy simulation when the upward surface sensible heat flux is terminated. Their results show that the decay of turbulent kinetic energy and temperature variance scales are related to the dimensionless time  $tw_*/z_i$ , where  $w_*$  is the convective vertical velocity scale and  $z_i$  the height of the ABL top.

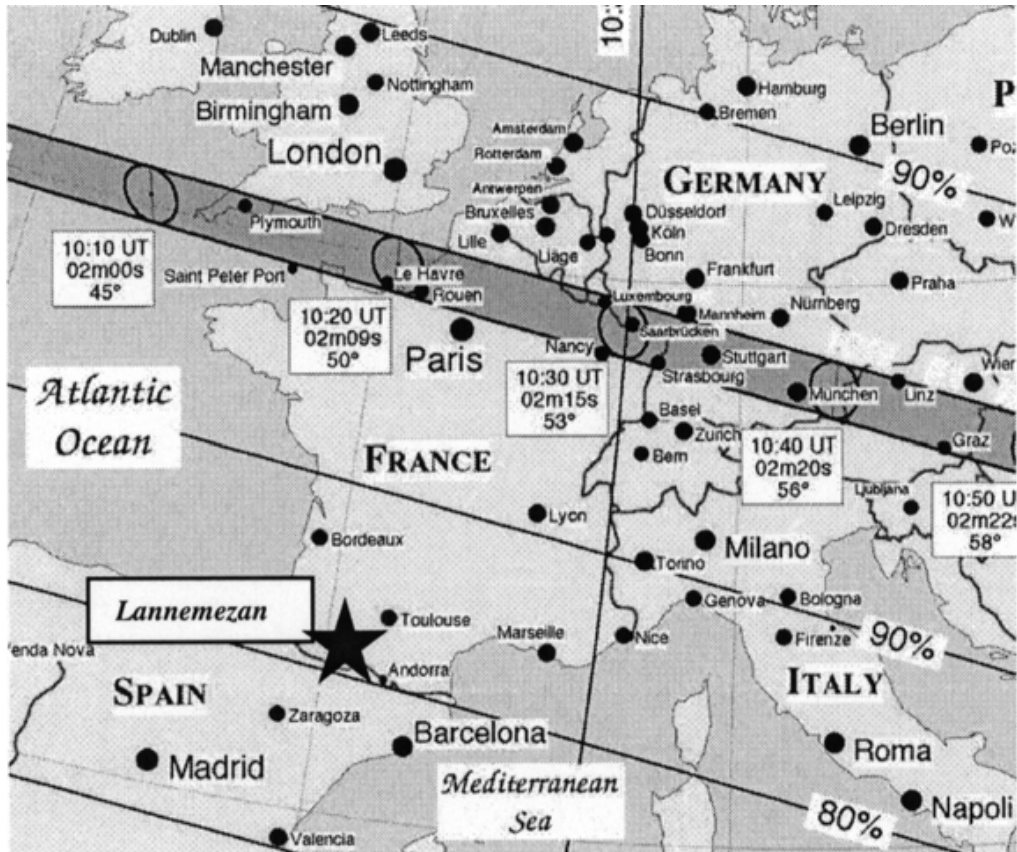


Figure 1. Map of the 11 August 1999 eclipse totality band in Europe. The research site is shown with a star in southwest France. Eclipse predictions and map courtesy of Fred Espenak, NASA/GSFC (website: <http://sunearth.gsfc.nasa.gov/eclipse/TSE2001/TSE2001.html>).

Above the ABL, observations of Kelvin–Helmoltz waves have been reported during various eclipses (see, for example, Davis and Da Rosa, 1970; Eaton et al., 1997).

In Europe (Figure 1), on 11 August 1999, the solar eclipse analyzed here was total in a band 116 km wide, extending from Cornwall in the U.K. at 1010 UTC to the Romanian Coast at 1110 UTC, and through northern France. Crochard and Renaut (1999) reported the effect of the eclipse on standard meteorological parameters such as solar radiation, shelter temperature, humidity and wind along the path of totality in France. The only clearly detectable effect is a temperature drop, varying with cloud cover. Morecroft et al. (2000) described solar radiation and temperature at the Wytham Environmental Change Network site (Oxfordshire, England), where the eclipse reached 96% of totality. Their measurements show a temperature fall more important over bare soil than over grass. The temperature minimum appeared about 15 min after the eclipse maximum. Piriou and Lamboley (1999) used a numerical approach (ARPEGE model) to assess the meteorological impact of eclipses at the local, regional and global scales. Different simulations (with and without clouds, with and without eclipse) show a local temperature change with a certain delay suggesting a rather strong thermal inertia of the atmosphere. Simulations also show a significant impact of the eclipse on temperature and wind at large scales.

De Wekker et al. (2000) described the effects of the solar eclipse on ABL processes in an alpine Swiss valley (95% totality). Their data show a strong reduction of the incoming radiation, sensible heat flux and stability near the surface. The flow regime in the valley is affected by the solar eclipse and the upslope flows along the valley-sides decrease, stop and reverse generating a subsequent decrease of convective activity.

During that solar eclipse, measurements were made at a research site in Campestrous on the Lannemezan plateau (43°08' N, 00°22' E, 593 m above sea level, located 30 km north of the Pyrenees mountains that reach 3000 m height), with a UHF-RASS radar (observations from 75 m up to 3000 m), a sodar (50 m up to 800 m) and an instrumented mast (0–60 m). This site, located about 800 km from the centre of totality band, was inside the 80% totality area. Note that this place is close to the Greenwich meridian, so that UTC and LST (Local Solar Time) differ only by less than 2 min. The eclipse began at 0858 UTC (first contact), reached its maximum obscuration at 1018 UTC and ended at 1143 UTC (last contact). Because of the relative positions and motions of Earth, Sun and Moon, the time between the beginning and the maximum obscuration (1 h 20 min) is shorter than the time between the maximum to the end of the eclipse (1 h 25 min). During that day, a synoptic weak and humid westerly Atlantic flow was responsible for a fair weather cumulus layer over France associated with cirrus clouds over some places (Crochard and Renaut, 1999). Fortunately, southern France was less affected by the cloud cover. The eclipse impact was stronger than the cloud shadowing effects.

In this study, we document and analyze the dynamic and thermodynamic response of the lower atmosphere, from the surface up to the top of the ABL, to the sudden change of the incoming solar energy. The experimental facilities and the inferred parameters are described in Section 2. Section 3 examines the time evolution of the surface-layer energy structure, radiation budgets, stability and turbulence, and the time evolution of the convective mixed layer. Section 4 gives the discussion and conclusions.

## 2. Instrumental Facilities

The present analysis uses data from a Ultra High Frequency (UHF) radar with a Radio Acoustic Sounding System (RASS), a Doppler sodar and an instrumented tower equipped with temperature and humidity sensors, sonic anemometers, pyranometers and pyrgeometers for radiative budget analysis. These instruments were not deployed for the observation of the solar eclipse only, since they have run routinely for several years.

TABLE I

Radar parameters during the solar eclipse experiment.

UHF wind profiler characteristics	
Transmitted frequency	1238 MHz
Pulse repetition frequency	20 KHz
Peak power	4 kW
Number of FFT points	128
Radial resolution	75 m
Number of beams	5
Antenna size	4 m <sup>2</sup> each
Off-zenith beams angle	17°
Beamwidth	8.5°
Lower gate	31 m
Number of gates	50
Range gate spacing	57 m

## 2.1. UHF RASS WIND AND TEMPERATURE PROFILING

The UHF-band Doppler radar is a five-beam Degréane Electronique wind profiler. This instrument is devoted to the study and survey of the dynamic and thermodynamic properties of the ABL in clear air or rainy conditions. During the case study presented here, the radar frequency was 1238 MHz, with a 4 kW peak pulse power, a 20 kHz pulse repetition frequency and a 150 m pulse length (Table I). The vertical beam and the four oblique beams, with an off-zenith direction of 17° and at 90 degrees intervals in azimuth, have a beamwidth of 8.5°. Vertical profiles of the radar reflectivity, wind Doppler radial velocity, and Doppler spectral width for each beam were acquired every 5 min from a height of 31 m, with a 75 m radial range sampling. Radial velocity was obtained with a resolution of 0.1 m s<sup>-1</sup>. Data quality control and processing are based on a sophisticated vertical and temporal continuity consensus algorithm working over a running period of 30 min (Jacoby-Koaly, 2000; Girard-Ardhuin, 2001). The zenith-pointing beam radial velocity provides the air vertical velocity. The horizontal wind components are inferred from the measurements of the oblique and vertical beams assuming a homogeneous horizontal wind.

With these characteristics, the minimum detectable signal, at a range of 1 km and for an echo spectral width of 2 m s<sup>-1</sup>, represents -18.8 dBZ in reflectivity factor units, and  $1.8 \times 10^{-15}$  m<sup>-2/3</sup> in  $C_n^2$  units. Depending on the atmospheric conditions, the maximum height covered by the profiler is between 2 and 3 km. The atmospheric parameters measured by the UHF profiler have been extensively

validated during calibration campaigns (Dessens et al., 1997; Campistron et al., 1997). More details on radar operation, data acquisition and processing can be found in Jacoby-Koaly (2000) and Jacoby-Koaly et al. (2002).

In the UHF band, the source of the radar echoes in clear air is due to the wave scattering on air refractivity index irregularities at a scale corresponding to half the transmitted wavelength (Tatarskii, 1961). These irregularities are produced by spatial turbulent fluctuations of humidity and temperature. According to Ottersten (1969), the radar reflectivity is proportional to the structure constant  $C_n^2$  of the turbulent refractivity index field. High  $C_n^2$  values usually result from the conjunction of strong turbulent mixing and sharp vertical variations of temperature and/or humidity. These favourable conditions are met at the top of the ABL where a layer of maximum radar echoes is usually observed. This feature is used operationally to accurately infer the ABL depth (Angevine et al., 1994).

An important parameter which can be obtained from the measurement of the Doppler spectral width is the turbulence intensity. The spectral width is linked to the wind fluctuations within the radar resolution volume. These fluctuations are mainly due to turbulent mixing and to the mean vertical wind gradient. In the case of a dry convective ABL with moderate or weak winds, the biological contamination by bird and insect echoes is limited by the Merrit algorithm (Merrit, 1995). Jacoby-Koaly et al. (2002) have investigated the contributions of these and other factors to the spectral width. However, in spite of numerous possible broadening factors, turbulence accounts for most of the spectral width (about 80% in these studies), while shear and residual noise make up all the rest. Those UHF measurements are in good agreement with aircraft data, particularly when oblique beams are used (the turbulent kinetic energy dissipation rate  $\epsilon$  is measured by the UHF radar with a  $2 \times 10^{-4} \text{ m}^2 \text{ s}^{-3}$  bias and a linear correlation coefficient of 0.9, relative to aircraft observations, see Jacoby-Koaly (2000) and Jacoby-Koaly et al. (2002)). Therefore, the turbulent contribution to the spectral width can be extracted. It is then possible with some realistic assumptions to infer the turbulent kinetic energy dissipation rate  $\epsilon$ , which is one of the most fundamental parameters for understanding the ABL (Gossard et al., 1998).

For temperature measurements, the UHF profiler is equipped with four acoustic horns located near the UHF antenna. The acoustic wave, with a wavelength tuned at half that of the UHF radar, is emitted at vertical incidence in a beam with a  $9^\circ$  aperture (Table II). From the velocity of this ‘acoustic echo’ measured by the UHF radar, the air virtual temperature  $T_v$  is inferred since it is related to the intrinsic sound speed  $c_s$  (see, for example, Lataitis, 1993).

As  $c_s$  is the sound speed in still air, the sound velocity measured by the UHF must be corrected from the air vertical velocity also measured by the radar at the same time (North et al., 1973).  $T_v$  is also corrected for errors due to vertical reflectivity gradients (Görsdorf and Lehmann, 2000; Girard-Ardhuin, 2001), which is most useful for the low levels. The vertical profile of  $T_v$  is obtained from 31 m above ground level up to about 800 m height with a 75-m vertical resolution,

TABLE II  
RASS characteristics during the solar eclipse experiment.

Acoustic source characteristics	
Sound generation	Random frequency modulation
Transmitted frequency	2790 → 2860 Hz
Number of FFT points	128
Radial resolution	75 m
Beamwidth	9.0°
Lower gate	31 m
Number of gates	20
Range gate spacing	60 m

10 min time resolution and an accuracy of about 0.5 °C (Girard et al., 1999; Girard-Ardhuin, 2001).

## 2.2. DOPPLER SODAR MEASUREMENTS

The Remtech PA2 sodar is used to measure the wind and turbulence near the ground in the range 0–200 m, which is not correctly sounded by the UHF radar. Located nearby the UHF wind profiler, its transmitted frequency is 2100 Hz, the lower gate and range gate spacing are 50 and 60 m respectively. Sodar measurements, used from 50 to 800 m above the ground, provide the echo strength proportional to the temperature structure constant  $C_t^2$ , the horizontal wind speed and direction, the vertical velocity and its standard deviation  $\sigma_w$ , averaged over 20 minutes. The sodar vertical velocity variance and horizontal wind measurements have been validated with sonic anemometer observations and radiosoundings, respectively (Dessens et al., 1997; Jacoby-Koaly, 2000). In typical convective ABL conditions, a good agreement is obtained for vertical velocity variance.

## 2.3. SURFACE AND MAST MEASUREMENTS

Kipp and Zonen pyranometers and pyrgeometers located at 1.5 m above the ground, provide the radiation fluxes (upward and downward visible between 0.3 to 3  $\mu\text{m}$ , and upward and downward infrared between 5 to 50  $\mu\text{m}$  respectively). Original data acquired at a frequency of 1 Hz are averaged over 10 minutes to evaluate the net radiation flux.

Two Metek sonic anemometers located at 10 and 60 m height give the three components of the wind. The temperature is deduced from the sound speed sampled every 0.05 s. The mean parameters, variances and covariances are estima-

TABLE III

The instruments and their respective measurements.

	Radar UHF with RASS 75–3000 m	Sodar 50–800 m	Sonic anemometer 10 and 60 m height	Temperature sensors 0.1, 2, 10 and 60 m height	Ground level station 2 m height (except 10 m for wind)
Reflectivity $C_n^2, C_T^2$	*	*			
ABL depth $z_i$	*				
Wind $\vec{V}, \ \vec{V}\ $	*	*	*		*
Vertical velocity $w$	*	*	*		
Temperature $T, T_v$	*		*	*	*
Radiation vis., infrared					*
Sensible heat flux $Q_H$			*		
Turbulence $\sigma_w, \epsilon, \sigma_T$	*	*	*		

ted every 10 min. From these measurements, the turbulent virtual heat flux is evaluated by the eddy correlation method

$$Q_H = \rho C_P \overline{w' \theta'_v}, \quad (1)$$

where  $\rho$  is the air density,  $C_P$  the specific heat capacity at constant pressure,  $w'$  the vertical velocity turbulent fluctuations and  $\theta'_v$  the potential virtual temperature turbulent fluctuations. The temperature gradient is deduced from three sensors (type Pt 1000) located at 0.1, 2, 10 and 60 m height and giving the temperature profile every second with an accuracy of 0.01 °C. The data are averaged over 10 min.

Table III summarizes the data measured by the different instruments.

### 3. Description and Analysis of the Solar Eclipse Case Study

#### 3.1. EVOLUTION OF THE SURFACE ATMOSPHERIC BOUNDARY LAYER

The net radiation flux determined from the downward and upward short and long wave radiation fluxes is balanced by the sensible and latent heat fluxes and by the heat flux to the underlying soil. The diurnal cycle of the radiation flux is shown for the 14 August 1999, a normal day of the eclipse week and for the 11 August, the eclipse day (Figures 2a and 2b respectively). On both days, clouds caused the rapid fluctuations of the radiative components and the net radiation flux measurements.

On the normal day (Figure 2a), the general trend is a net radiation flux increase between 0500 and 1200 UTC, followed by a regular decrease, well correlated with the incoming visible radiation. Since the infrared radiation variations depend on the total sky temperature for downward long waves and of the ground temperature for upward long waves, they are low ( $30\text{--}40\text{ W m}^{-2}$ ) and mainly related to the clouds. Thus, during daytime, the net radiation, inferred from the four measurements, follows the incoming visible radiation evolution.

On 11 August (Figure 2b), after a typical increase between 0500 to 0858 UTC, the net radiation flux gradually declines from  $400\text{ W m}^{-2}$  at the first contact of the solar eclipse until the maximum obscuration (1018 UTC,  $40\text{ W m}^{-2}$ ). After the minimum, the flux grows from 40 to  $650\text{ W m}^{-2}$  until the last contact. Then, the net radiation flux decreases regularly in the afternoon, as on a normal day. The net radiation flux evolution follows the downward visible flux, with a minimum at the time of the eclipse maximum. When the obscuration is maximum, the incoming solar radiation and the net radiation flux are almost completely cut off. The infrared radiation does not seem to be really affected by the eclipse phenomenon. Stewart and Rouse (1974) have found a decrease of net radiation flux related to the nature of the surface (lake, swamp, ridge). Their results show evident longwave radiation fluctuations due to the eclipse that do not appear in our measurements.

As the net radiation flux, the sensible heat flux grows until the first contact of the eclipse (Figure 3) and decreases to  $5\text{ W m}^{-2}$  at 1020 UTC after the eclipse maximum, instead of about  $150\text{ W m}^{-2}$  at the same time on the other day. After this minimum, the flux increases rapidly until the end of the eclipse. After the eclipse period, the sensible heat flux seems not to be affected during the end of the day and recovers normal cloudy day values. This evolution is in agreement with Eaton et al.'s (1997) and Stewart and Rouse's (1974) results, which do not present a noticeable time lag, the sensible heat flux minimum being quasi-instantaneous with the eclipse maximum. Measured fluctuations in the sensible heat flux are due to passing clouds. In particular the high value of sensible heat flux just before the eclipse maximum (about  $60\text{ W m}^{-2}$ , Figure 3), corresponds to an increase of the net radiation that can be explained by the temporal variation of the cloud cover.

The diurnal cycles of the net radiation flux and the sensible heat flux show that the sensible heat flux clearly follows the evolution of the net radiation flux

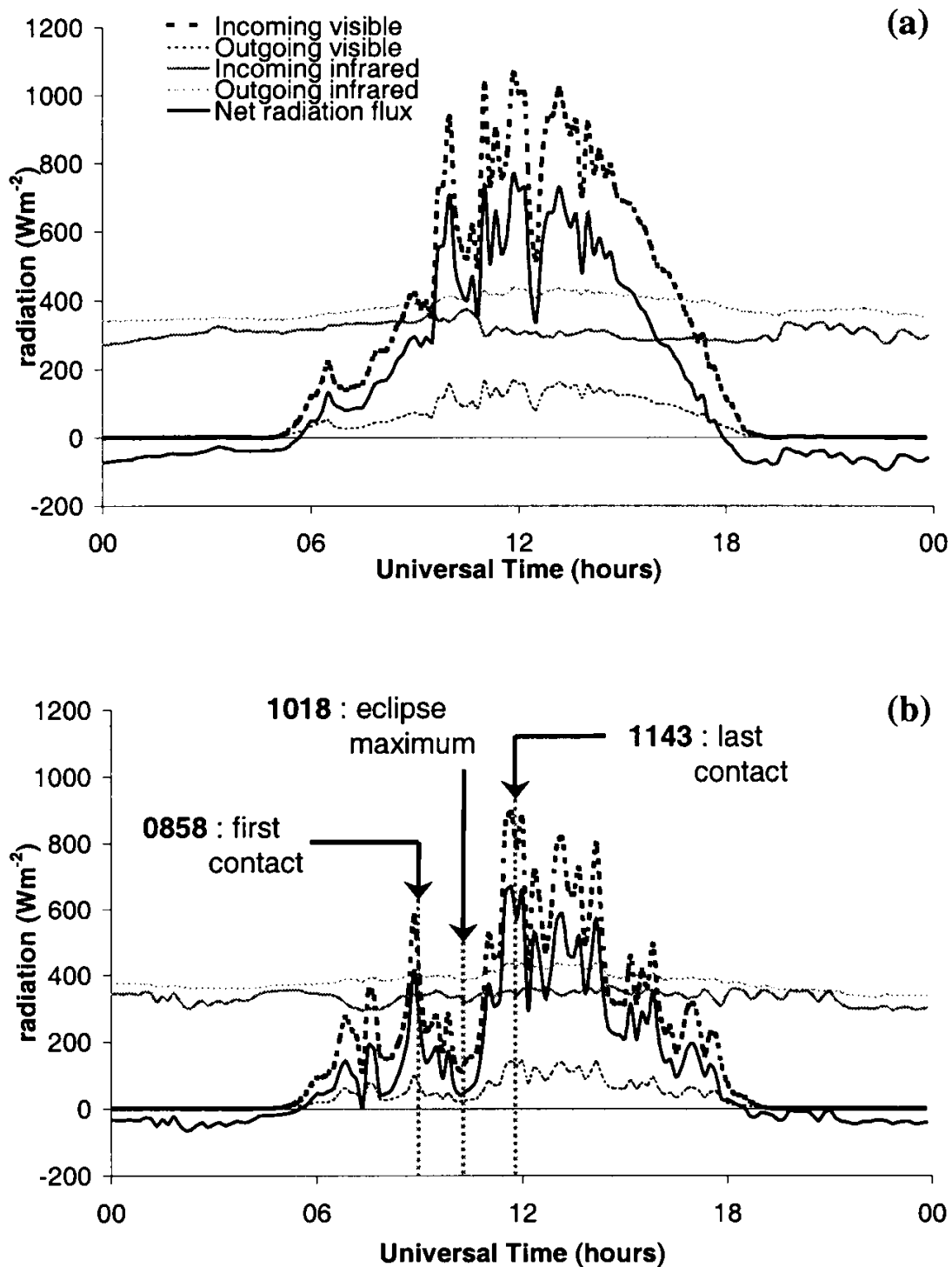


Figure 2. Evolution of the net radiation flux and its components for (a) a reference day (14 August 1999), and (b) for the eclipse day (11 August 1999). In (b), the first arrow represents the first contact of the eclipse, the second one the maximum obscuration, and the third one the last contact of the eclipse.

during the eclipse, which cuts the energy supply to a conventional development of a convective ABL.

As reported by Segal et al. (1996) for a morning eclipse, the evolution of the air temperature is characterized by three stages: stabilization of the temperature between the first contact and the eclipse maximum (except at 0.1 m above the ground), temperature decrease after the eclipse maximum and temperature in-

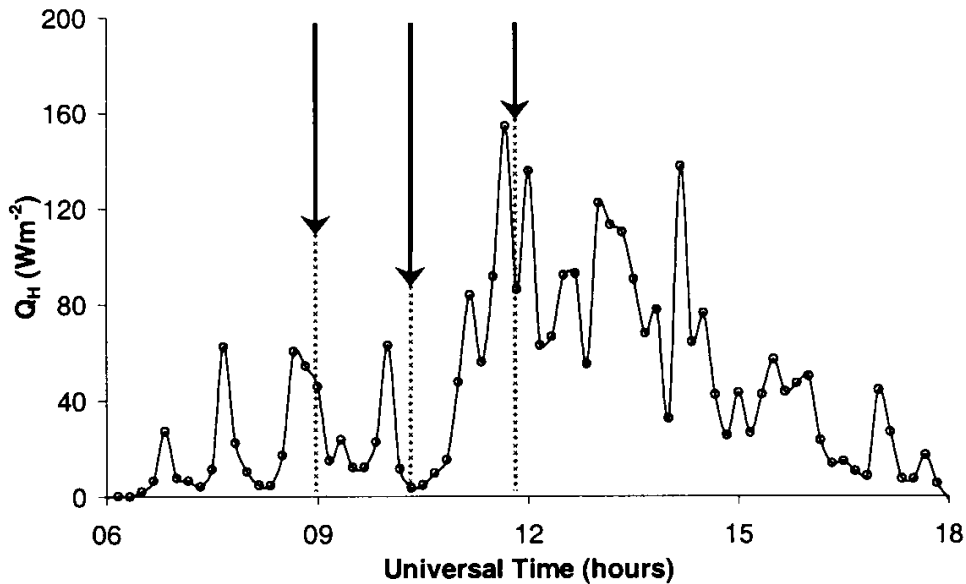


Figure 3. Sensible heat flux evolution from the sonic anemometer at 10 m during the eclipse day. Arrows have the same meaning as in Figure 2.

crease. These three stages are clearly apparent in the present observations of the potential temperature evolution (Figure 4a). We can note particularly the different behavior of the temperature observed at the lowest measurement level compared to the levels above. Whereas there is a continuous decrease of the temperature at 0.1 m after the eclipse onset, a distinct temperature stabilization affects the three upper levels (2, 10 and 60 m) before the eclipse maximum. Also, the temperature variation amplitude decreases as a function of height above the ground because the temperature in the ABL is mainly controlled by the thermal exchange originating from the solar energy absorption by the ground. During the eclipse, instability decreases near the ground until 60 m and the convective layer becomes neutral to stable (Figure 4a). This evolution is related to a reduction of the turbulent vertical exchanges also revealed by the reflectivity and turbulence UHF observations discussed below.

The temperature difference between the measured minimum and the temperature interpolated at the same time between the previous maximum and the next maximum, are 7, 1.3, 1.2 and 1.0 °C for 0.1, 2, 10 and 60 m height respectively. These values are comparable to the measurements at 2 m height in the totality band during this eclipse, showing a temperature fall of 0.8–2.7 °C (Crochard and Renault, 1999). Morecroft et al. (2000) find a 2.4–4.5 °C fall at 96% totality. The temperature fall depends, among other factors, on the height, the ground cover (bare soil or vegetation), the ground humidity (wet or dry soil), the latitude, the sun inclination and the hour of the eclipse as shown by the measurements made on different sites, as over the Arctic ice with a temperature fall of 10 °C (Stewart and Rouse, 1974), or over a soil surface in a clear air with a temperature decrease of 7 °C (Eaton et al., 1997), or over a grass surface with a 4.5 °C temperature fall (Morecroft et al., 2000).

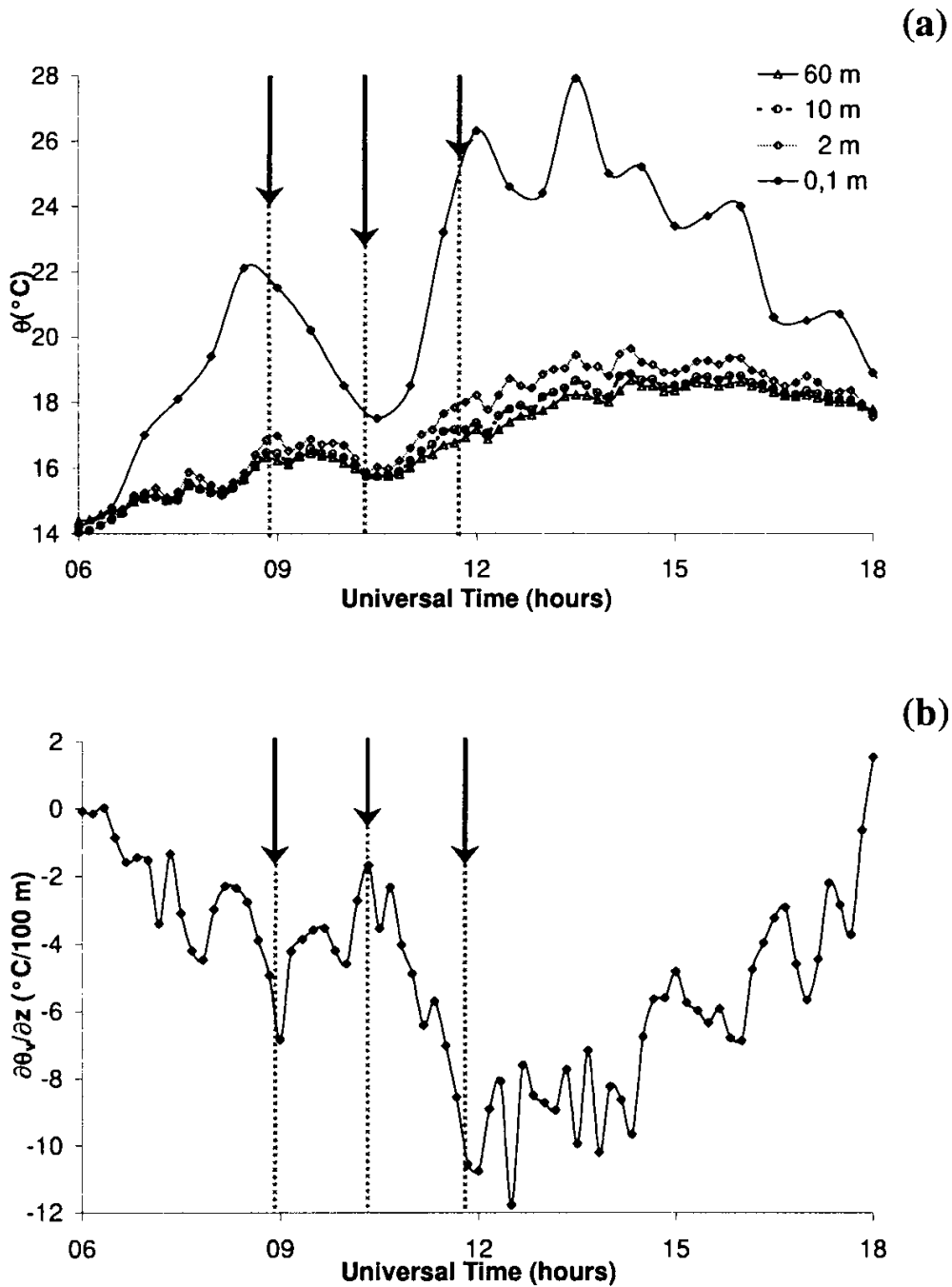


Figure 4. Potential temperature evolution during the eclipse day (a) from mast sensors at 0.1, 2, 10 and 60 m height and evolution of  $\partial\theta_v/\partial z$  (b) between 2 and 10 m height. Arrows have the same meaning as in Figure 2.

The gradient of the potential virtual temperature, inferred from the mast measurements at 2–10 m height (Figure 4b), decreases from 0 at 0600 UTC to  $-6.8$  °C/100 m at 0900 UTC with some fluctuations due to the cloudiness, showing the instability of the surface layer. As the eclipse starts, this trend reverses:  $\partial\theta_v/\partial z$  increases to  $-1.7$  °C/100 m corresponding to the eclipse maximum with a possible time lag of a few minutes. The reduction of the thermal instability at the same hour is about 8 °C/100 m in comparison with a normal day. After the eclipse maximum time, the thermal instability reinforces until 1200 UTC with a strong negative temperature gradient reaching  $-11.8$  °C/100 m. The afternoon is marked

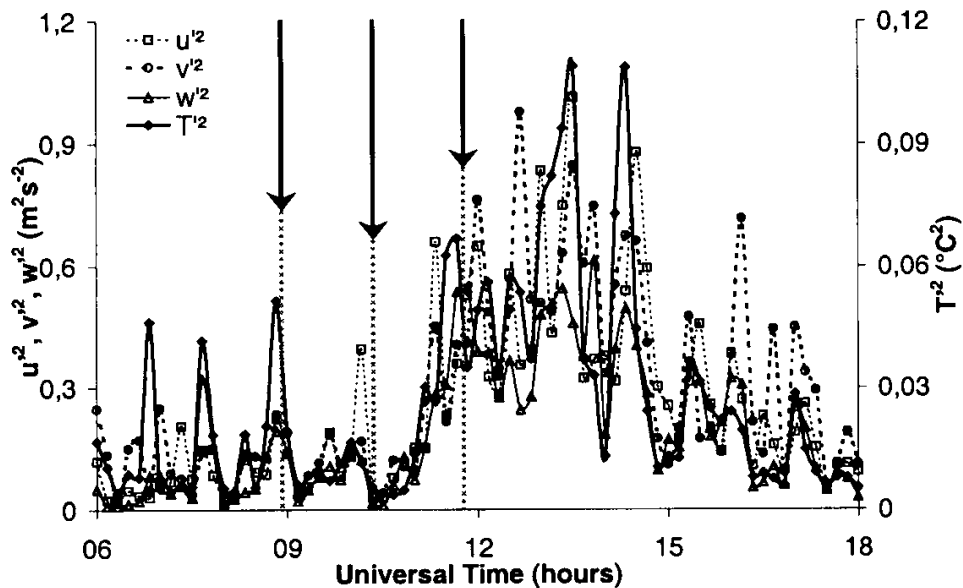


Figure 5. Evolution of the variances of the three wind components and the temperature (the scale is on the right for this term). Arrows have the same meaning as in Figure 2.

by a decrease of the thermal instability. In the surface layer, the eclipse tends to attenuate the thermal instability started from the beginning of the day. The instability, strong close to the ground, is moderated, indeed even nullified, around the obscuration maximum. This result is in agreement with previous studies and the net radiation decrease. Temperature measurements during the 10 May 1994 eclipse at 89% totality in the surface layer show a strong decrease of the thermal instability during a period of 45 min centered on the eclipse maximum (Segal et al., 1996; Eaton et al., 1997).

The variances of the three components of the wind measured at 60 m height (Figure 5) are weak until 1030 UTC, corresponding to the eclipse maximum and then increase. Observed variances fluctuate more before the eclipse than from the first contact to the eclipse maximum. Eaton et al. (1997) show very different values between the variance of the vertical velocity and the others and a sharp decrease during the eclipse event. The temperature variance decreases sharply from the eclipse beginning until 1030 UTC, then increases as in a normal convective day. This parameter follows the evolution of the other variances.

### 3.2. EVOLUTION OF THE MEAN PARAMETERS IN THE MIXED LAYER

As described in Section 2, the reflectivity parameter  $C_n^2$  is linked to the surface sensible and latent heat fluxes and it increases at the top of the ABL. This feature is well observed on the UHF data. The UHF radar, unlike 10-cm radars for example, is less sensitive to biological tracers (insects, birds).

On 11 August, the top of the convective ABL (Figure 6a, dots) corresponding to the maximum value of  $C_n^2$ , reaches its maximum at about 1200 m height at 0930 UTC. After that time, the maximum value of reflectivity decreases sharply with a minimum at 1045 UTC, corresponding to a 10 dB reduction about 25 min

after the eclipse maximum. The reflectivity increases again after the end of the eclipse. Likewise inside the ABL,  $C_n^2$  decreases during the eclipse, and recovers larger values in the afternoon. This attenuation of  $C_n^2$  during the solar eclipse is related to the decrease of turbulence and sensible heat flux in the surface layer, as noted by Rabin and Doviak (1989). Below 300 m, the sodar data (Figure 7a) follow the same pattern, with reflectivity increasing until 0900 UTC, decreasing sharply from more than 60 dB at 0830 UTC at 200 m height to about 10 dB at 1045 UTC, corresponding to the eclipse maximum, and increasing again after 1100 UTC.

Both instruments show an abnormally reduced reflectivity during the eclipse throughout the ABL after the maximum obscuration. This result agrees with observations by Eaton et al. (1997), showing the same decrease of  $C_n^2$  during the eclipse, and with Rabin and Doviak's (1989) results suggesting that the minimum  $C_n^2$  occurred 30 min after the maximum obscuration.

After the eclipse, the ABL subsides due to the synoptic situation as shown on the time evolution of the wind speed (Figure 6b). The wind profiles measured by the UHF radar (Figures 6b and 6c) present a clear limit between the ABL and the atmosphere above it. From the ground to the top of the ABL, the wind is weak, about 2–5 m s<sup>-1</sup>, particularly in the morning, as confirmed by the sodar data (Figure 7b), but reaches 10–16 m s<sup>-1</sup> above the ABL (Figure 6b). The wind is westerly (Figure 6c) at upper levels and northeasterly at lower levels (Figure 7c). There is no evidence that the eclipse has affected the wind in this case, as in the case presented by Eaton et al. (1997). A numerical sensitivity study applied to the eclipse of 11 August 1999 shows a weak influence on the wind at 10 m height with differences in sea and mountain breezes (Piriou and Lamboley, 1999), which is difficult to verify in our example, but the data collected in the totality band did not reveal any effect (Crochard and Renaut, 1999).

The time evolution of the virtual temperature  $T_v$  derived from the RASS from 60 to 1000 m height (Figure 8) illustrates, once again, the strong impact of the eclipse on the diurnal cycle. Before the first contact,  $T_v$  increases regularly, simultaneously with the net radiation flux (Figure 2b), then decreases slightly above 300 m and starts increasing again within 30 minutes after the eclipse maximum, following again the normal diurnal temperature cycle. The decrease of temperature (Figure 9a) around the eclipse maximum is stronger in the surface layer than at higher levels (0.7 °C only at 600 m), but the data do not resolve a possible time lag between the surface layer and the top of the ABL. The local minimum in temperature, at all levels, occurs about 15 min after the eclipse maximum. This time lag, approximated by the data analysis procedure, is comparable to the 5–10 min reported by Segal et al. (1996) in similar conditions and to the 15 min reported by Crochard and Renaut (1999) and by Morecroft et al. (2000) for the same event. Before 1200 UTC, the potential virtual temperature  $\theta_v$  evolves almost in the same way at all levels of the ABL, with a gradient close to the adiabatic profile. A slightly stable profile is destabilized by convection below 300 m (Figure 9b), following

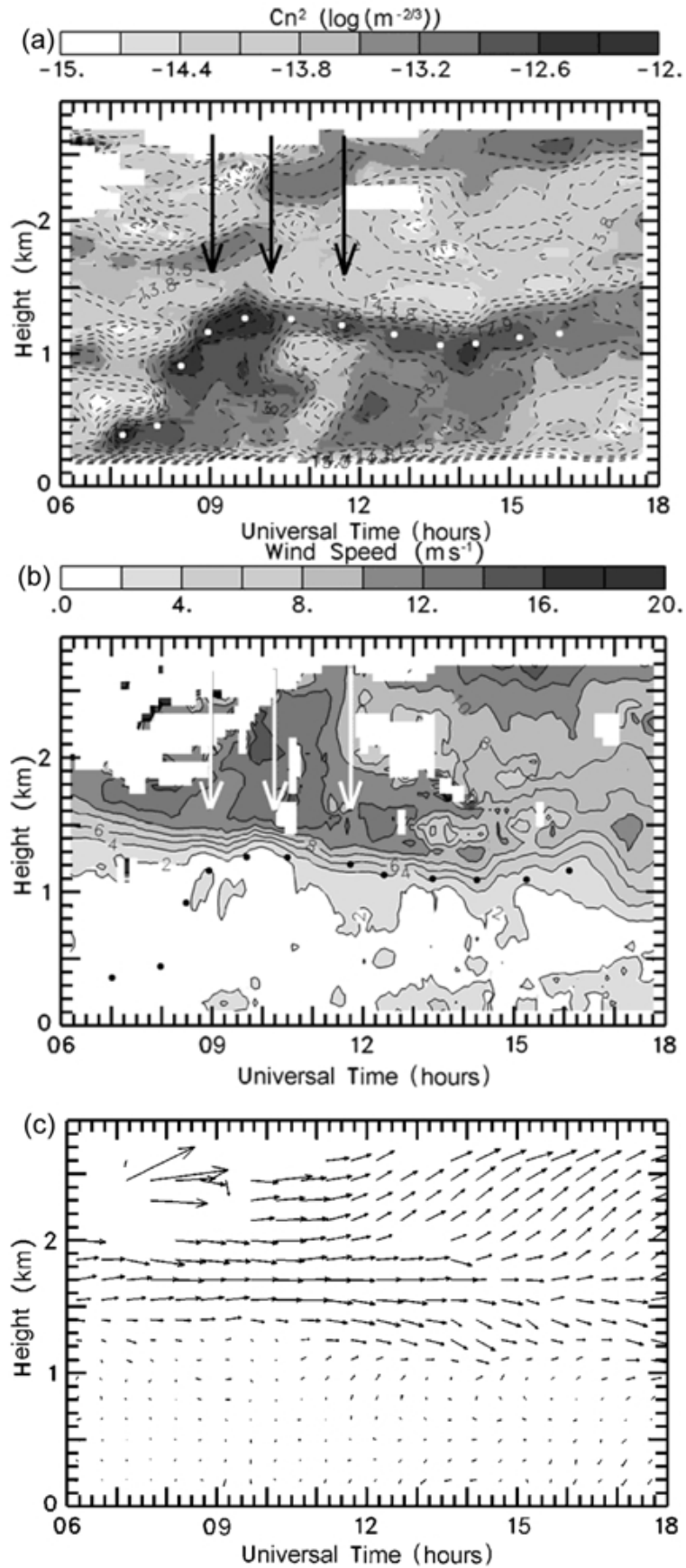


Figure 6. Reflectivity (a), wind speed (b), and wind direction (c) evolution inferred from the UHF radar. Dots indicate the top of the convective boundary layer inferred from (a). Arrows have the same meaning as in Figure 2.

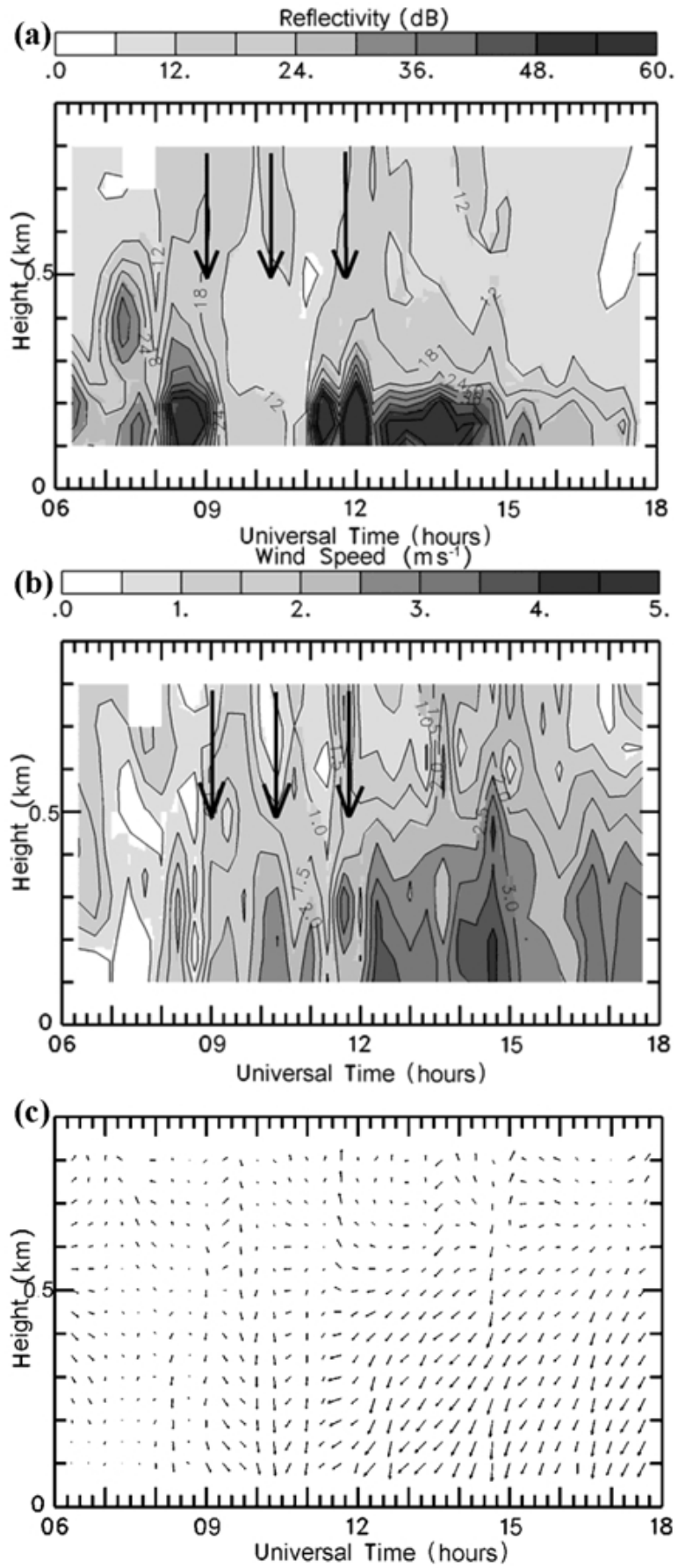


Figure 7. Same as in Figure 6, but for the sodar.

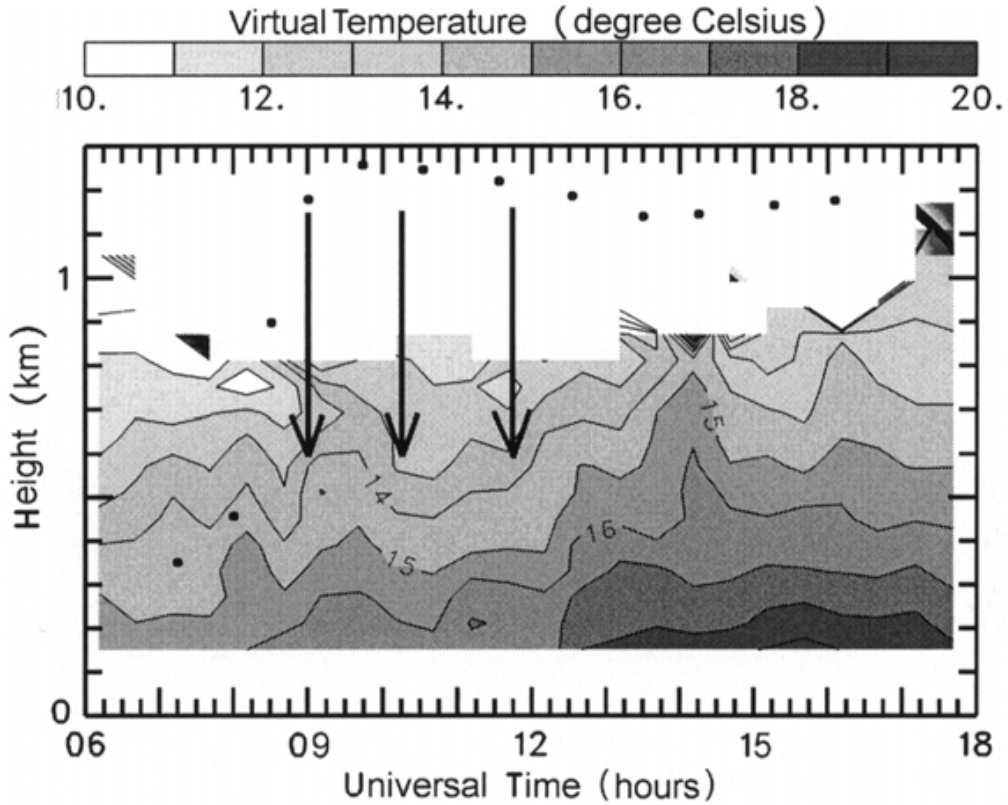


Figure 8. Virtual temperature evolution inferred from the RASS data. Dots have the same meaning as in Figure 6. Arrows have the same meaning as in Figure 2.

the normal diurnal cycle, until it is re-stabilized around the eclipse maximum and destabilized again as the obscuration decreases.

### 3.3. EVOLUTION OF THE TURBULENCE IN THE MIXED LAYER

The turbulence structure inside the ABL is illustrated by the standard deviation of the vertical velocity  $\sigma_w$  observed with the sodar and the dissipation rate  $\epsilon$  derived from the spectral width of the UHF radar vertical velocity.

As for  $C_n^2$ , the diurnal evolution of  $\sigma_w$  is affected by the eclipse with a reduction by one order of magnitude around the eclipse maximum (Figure 10a). This reduction occurs at all levels sounded by the sodar and  $\sigma_w$  is roughly uniform from 100 to 600 m throughout the eclipse period (Figure 10b). The evolution of  $\sigma_w$  shows that the turbulence inside the ABL is strongly modified during the duration of the eclipse.

$\epsilon$  follows the same general pattern as  $\sigma_w$  (Figures 11a, b), showing that the UHF radar gives a reliable estimation of the dissipation rate inside the ABL (Jacoby-Koaly, 2000; Jacoby-Koaly et al., 2002). After a classical development of the turbulence in the ABL from 0800 to 0930 UTC with a maximum value of  $\epsilon$  near 200 m height, the turbulence is sharply suppressed after 0945 UTC near ground level. Around the eclipse maximum until the last contact,  $\epsilon$  is reduced by one order of magnitude close to the ground. The turbulence reduction propagates over a period of 30 min across the ABL from the ground to the top.  $\epsilon$  increases in the

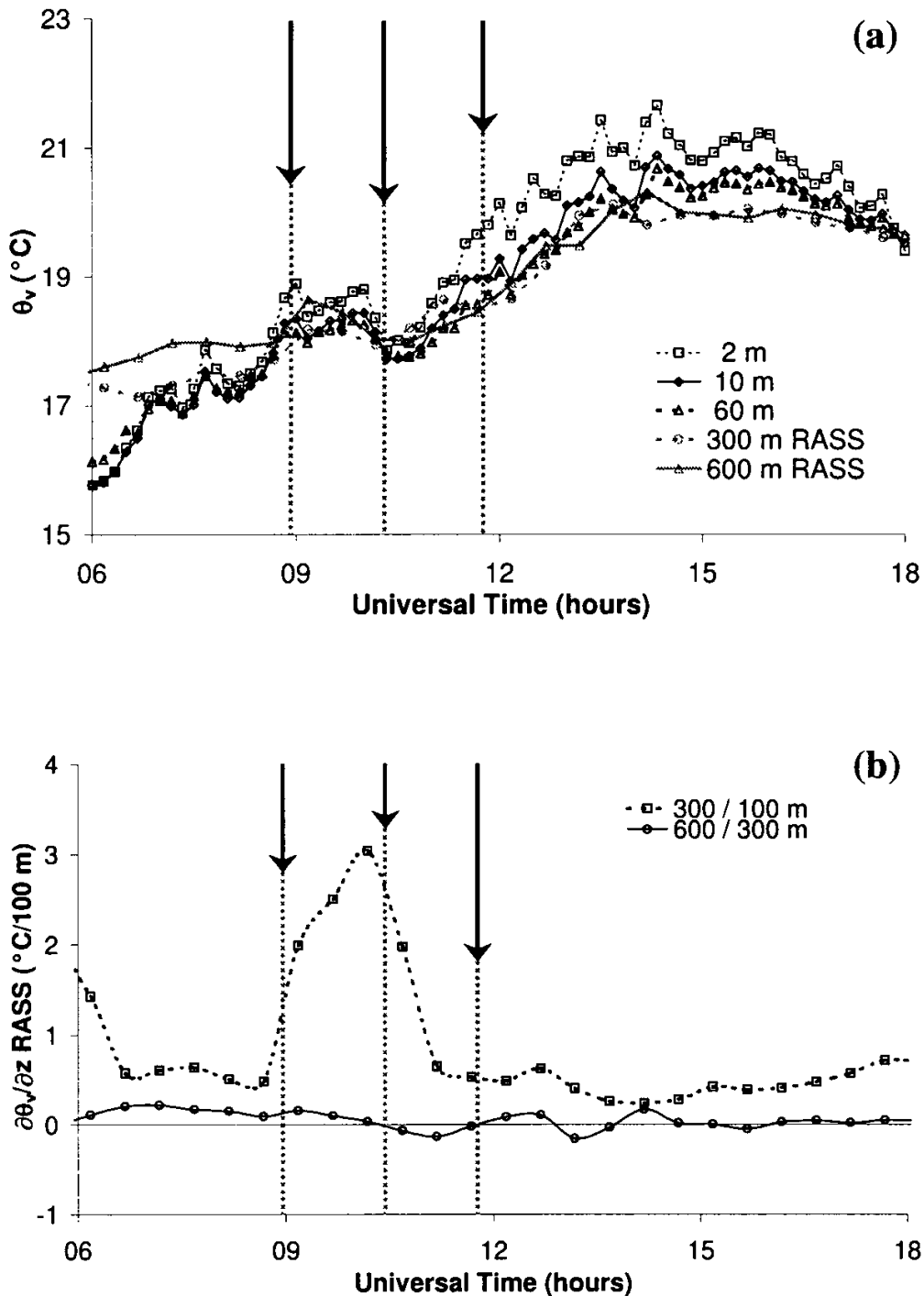


Figure 9. (a) Evolution of the virtual potential temperature from mast sensors at 2, 10 and 60 m height and from RASS at 300 and 600 m height (b); evolution of  $\partial\theta_v/\partial z$  between 100 and 300 m and between 300 and 600 m height (RASS measurements). Arrows have the same meaning as in Figure 2.

afternoon with lower values than before the event. The turbulent kinetic energy deduced from mast measurements at 10 m, has then exactly the same evolution as the sensible heat flux (Figure 3), proving that the thermal turbulence is higher than the mechanical turbulence for this case. The evolution is the same as for the radar time series, except for the values of the peaks. The eclipse tends to strongly decrease the turbulence inside the convective ABL up to the top, this sharp decrease

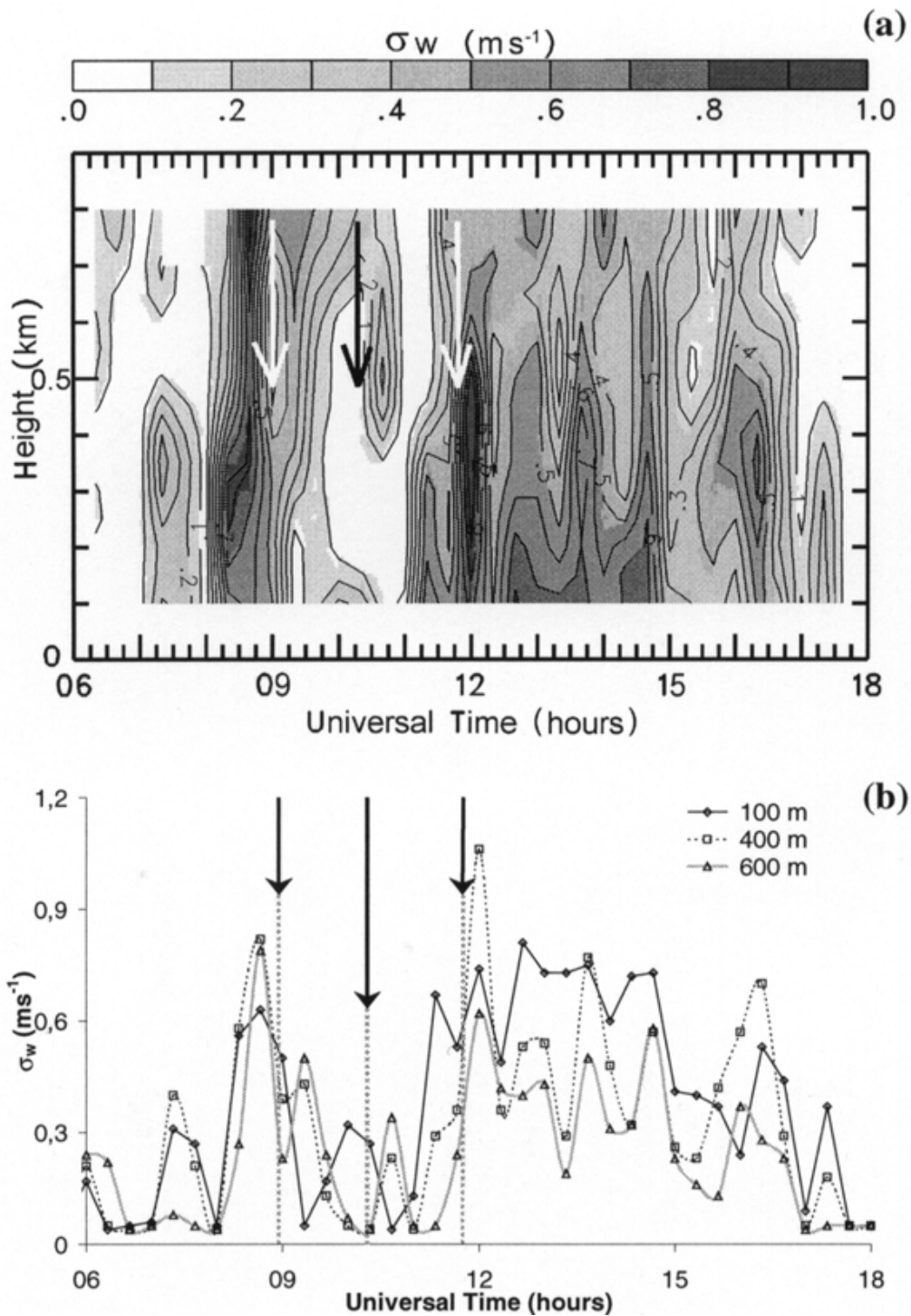


Figure 10. Spectral width evolution inferred from the sodar: (a) Time-height diagram and (b) time-series at 100, 400 and 600 m height. Arrows for both diagrams have the same meaning as in Figure 2.

was also reported by Eaton et al. (1997). The same phenomenon appears after the eclipse maximum when the increase in turbulence again propagates from the ground to the ABL top over a period of 15 min.

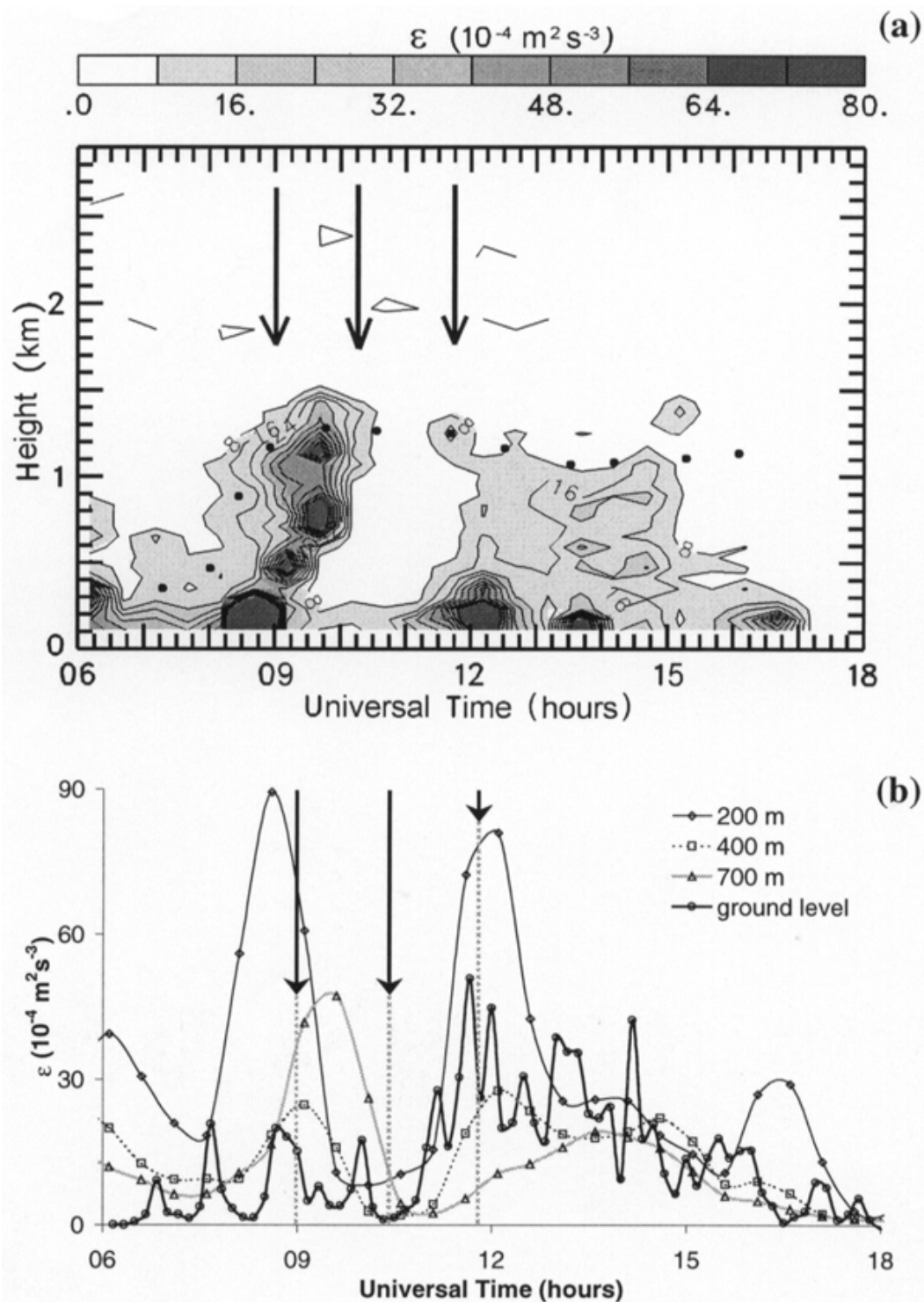


Figure 11. Evolution of the turbulent kinetic energy dissipation rate from the UHF radar: Time-height diagram (a) and time series (b) at 200, 400 and 700 m height. Ground level data are inferred from mast measurements at 10 m. Dots in (a) have the same meaning as in Figure 6. Arrows have the same meaning as in Figure 2.

#### 4. Discussion and Conclusion

A near total solar eclipse (80%) was observed on 11 August 1999 using mast and ground instruments, and a UHF-RASS radar providing high spatial and temporal resolutions. This radar gave continuous observations over a large vertical

range (3 km), across the entire ABL. This is the first time that such measurement have been obtained, giving evidence of the influence of an eclipse on the atmosphere, and revealing a significant impact up to the top of the convective ABL, with turbulence impacts lagging 15–30 min behind the evolution of the solar radiation.

The surface-layer evolution on this day is quite different from a typical convective cloudy day since the solar radiation is strongly reduced during the 3 h when convective activity would have normally increased. The reduction of the solar radiation during these 3 h cuts the energy supply needed for ABL development. The sensible heat flux is reduced to almost zero and thermal instability and turbulence are strongly attenuated around the maximum obscuration. As a result, all mean and turbulent parameters in the ABL are affected by the solar eclipse.

The first consequence of the eclipse is the large reduction and increase of the net radiation between the first contact and the maximum of the eclipse, and between the maximum and the last contact, respectively. The variations measured here ( $-300 \text{ W m}^{-2}$  and  $450 \text{ W m}^{-2}$  per hour, respectively) are three times greater than the values generally encountered during the afternoon/night and night/morning transitions, respectively. The ABL temperature is reduced by  $4.6\text{--}0.6 \text{ }^\circ\text{C}$  up to the top of the ABL, and the thermal gradient is strongly modified in the surface layer below 300 m. Temperature evolves through three stages (stabilization, reduction, and increase) that correspond to three regimes of stability (Segal et al., 1996). There is no perceptible effect on the horizontal wind field.

The consequences of the eclipse on the ABL turbulent structure are characterized near the ground by a reduction of the sensible heat flux ( $-140 \text{ W m}^{-2}$ , with a rate of change of  $-40 \text{ W m}^{-2}$  per hour) and of the other turbulence parameters from the first contact to the maximum of the eclipse. The turbulent energy dissipation is reduced by 90% inside the ABL and the reflectivity decreases by 10 dB in the entire ABL. The UHF measurements show clearly that the turbulent kinetic energy dissipation rate decreases in altitude after decreasing at ground level. The average time lag between the minimum of  $\epsilon$  at ground level and at 700 m height is about 30 min, giving an estimation of the propagation time between the ground and the top of the ABL. It is comparable to the convective turbulence decay time at the first contact of the eclipse, given by Nieuwstadt and Brost (1986),  $t = z_i/w_*$ , which in our case is 15 min. Whereas Nieuwstadt and Brost (1986) predicted that the vertical velocity variance decreases faster than the horizontal velocity variances, no anisotropy can be clearly identified in the present observations.

Between the maximum and the last contact, the growth of the net radiation ( $450 \text{ W m}^{-2}$  per hour), and the sensible heat flux ( $120 \text{ W m}^{-2}$  per hour) progressively generates turbulence across the ABL, with a surface to altitude time lag similar to the one observed between the first contact and the eclipse maximum. The turbulent intensity stays relatively low after the eclipse, a possible consequence of the loss of radiative energy during the 3-h long eclipse.

The data set presented here give a comprehensive description of the response of the ABL to a rapid modification of the surface forcing, and should provide a

valuable test of the aptitude of numerical models to describe the mean and turbulent motions in comparable situations.

## Acknowledgements

This work was funded by the 'Agence De l'Environnement et de la Maîtrise de l'Energie' (ADEME) and 'Electricité De France' (EDF, grant B01826). We are grateful to F. Ardhuin for useful reviews.

## References

- Angevine, W. M., White, A. B., and Avery, S. K.: 1994, 'Boundary-Layer Depth and Entrainment Zone Characterization with a Boundary-Layer Profiler', *Boundary-Layer Meteorol.* **68**, 375–385.
- Campistron, B., Bénech, B., Dessens, J., Jacoby-Koaly, S., Dupont, E., and Carissimo, B.: 1997, 'Performance Evaluation of a UHF Boundary Layer Radar in Raining Conditions Based on Disdrometer Measurements', in *8th International Workshop on Technical and Scientific Aspects of MST Radar*, Bangalore, India, December 15–20, 1997, pp. 334–337.
- Crochard, G. and Renaut, D.: 1999, 'L'impact Météorologique de l'Eclipse du 11 Août 1999', *La Météorologie*, 8ème série **28**, 57–63.
- Davis, M. J. and Da Rosa, A. V.: 1970, 'Possible Detection of Atmospheric Gravity Waves Generated by the Solar Eclipse', *Nature* **226**, 1123.
- Dessens, J., Bénech, B., Campistron, B., Jacoby-Koaly, S., Derrien, S., Dupont, E., and Carissimo, B.: 1997, 'A UHF Wind Profiler Validation Campaign Using Rawinsounding and Sodar Data', in *8th International Workshop on Technical and Scientific Aspects of MST Radar*, Bangalore, India, December 15–20, 1997, pp. 200–203.
- De Wekker, S. F. J., Steyn, D. G., Rotach, M. W., Andretta, M., and Zappa, M.: 2000, 'Effects of the 11 August 1999 on Boundary Layer Processes during the MAP-Riviera Field Study', in *Preprints of MAP Meeting*, Bohinjjska Bistrica, Slovenia, May 24–26, 2000, p. 119.
- Eaton, F. D., Hines, J. R., Hatch, W. H., Cionco, R. M., Byers, J., Garvey, D., and Miller, D. R.: 1997, 'Solar Eclipse Effects Observed in the Planetary Boundary Layer over a Desert', *Boundary-Layer Meteorol.* **83**, 331–346.
- Girard, F., Bénech, B., Campistron, B., Jacoby-Koaly, S., Dessens, J., Dupont, E., and Carissimo, B.: 1999, 'Characteristics of the Atmospheric Boundary Layer Observed with a UHF-RASS Wind Profiler', in *29th International Conference on Radar Meteorology*, Montreal, Canada, July 12–19, 1999, American Meteorological Society, pp. 480–483.
- Girard-Ardhuin, F.: 2001, *Utilisation d'un Radar UHF RASS pour l'Etude de la Couche Limite Atmosphérique en vue d'une Application à la Pollution Atmosphérique*, Ph. D. Dissertation, University of Toulouse, France, 215 pp.
- Görsdorf, U. and Lehmann, V.: 2000, 'Enhanced Accuracy of RASS-Measured Temperatures due to an Improved Range Correction', *J. Atmos. Oceanic Tech.* **17**, 406–416.
- Gossard, E. E., Wolfe, D. E., Moran, K. P., Paulus, R. A., Anderson, K. D., and Rogers, L. T.: 1998, 'Measurement of Clear-Air Gradients and Turbulence Properties with Radar Wind Profilers', *J. Atmos. Oceanic Tech.* **15**, 321–342.
- Jacoby-Koaly, S.: 2000, *Application d'un Radar Profileur de Vent UHF à l'Etude de la Couche Limite Atmosphérique*, Ph.D. Dissertation, University of Toulouse, France, 264 pp.
- Jacoby-Koaly, S., Campistron, B., Bernard, S., Bénech, B., Girard-Ardhuin, F., Dessens, J., Dupont, E., and Carissimo, B.: 2002, 'Estimation of the Turbulent Dissipation Rate from the Dop-

- pler Spectral Width Measured in the Atmospheric Boundary Layer by a UHF Wind Profiler: Comparison with In Situ Aircraft Data', *Boundary-Layer Meteorol.* **103**, 361–389.
- Lataitis, R. J.: 1993, *Theory and Application of a Radio Acoustic Sounding System (RASS)*, Ph.D. Dissertation, University of Colorado, CO, 207 pp.
- Merrit, D. A.: 1995, 'A Statistical Averaging Method for Wind Profiler Doppler Spectra', *J. Atmos. Oceanic Tech.* **12**, 985–995.
- Morecroft, M., Oliver, H., Stokes, V., and Morison, J.: 2000, 'Sensing and Mis-Sensing the Eclipse', *Weather* **55**, 174–176.
- Nieuwstadt, F. T. M. and Brost R. A.: 1986, 'The Decay of Convective Turbulence', *J. Atmos. Sci.* **43**, 532–546.
- North, E. M., Peterson, A. M., and Parry, H. D.: 1973, 'RASS, a Remote Sensing System for Measuring Low-Level Temperature Profiles', *Bull. Amer. Meteorol. Soc.* **54**, 912–919.
- Ottersten, H.: 1969, 'Atmospheric Structure and Radar Backscattering in Clear Air', *Radio Sci.* **4**, 1179–1193.
- Piriou, J.-M. and Lamboley, P. : 1999, 'Prévision Numérique des Effets Météorologiques d'une Eclipse de Soleil', *La Météorologie*, 8ème série **28**, 52–56.
- Rabin, R. M and Doviak, R. J.: 1989, 'Meteorological and Astronomical Influences on Radar Reflectivity in the Convective Boundary Layer', *J. Appl. Meteorol.* **28**, 1126–1235.
- Segal, M., Turner, R. W., Prusa, J., Bitzer, R. J., and Finley, S. V.: 1996, 'Solar Eclipse Effects on Shelter Air Temperature', *Bull. Amer. Meteorol. Soc.* **77**, 89–99.
- Stewart, R. B. and Rouse, W. R.: 1974, 'Radiation and Energy Budgets at an Arctic Site during the Solar Eclipse of July 10, 1972', *Arctic Alpine Res.* **6**, 231–236.
- Tatarskii, V. I.: 1961, *Wave Propagation in a Turbulent Medium*, McGraw-Hill, New York, 285 pp.